Cu(InGa)Se 2 Solar Cell Efficiency Enhancement Using a Yb-Doped SnO x Photon Converting Layer

Karima Bouras, Guy Schmerber, Gerald Ferblantier, Damien Aureau, Hyeonwook Park, Woo Kyoung Kim, Hervé Rinnert, Aziz Dinia, Abdelilah Slaoui, Silviu Colis

Cu(InGa)Se_2 solar cell efficiency enhancement using a Yb-doped SnO_x photon converting layer

Karima Bouras,* Gerald Ferblantier, and Abdelilah Slaoui

Laboratoire des sciences de l'ingénieur, de l'informatique et de l'imagerie (ICube), UMR 7357 CNRS and Université de Strasbourg, 23 rue du Loess, BP 20 CR, F-67037 Strasbourg Cedex 2, France

Hervé Rinnert

Institut Jean Lamour (IJL), UMR 7198 CNRS, Université de Lorraine, BP 70239, F-54506 Vandoeuvre-lès-Nancy, France

Damien Aureau

Institut Lavoisier de Versailles (ILV), Université de Versailles-St-Quentin, UMR 8180, 45 avenue des Etats Unis, 78000 Versailles, France

Hyeonwook Park and Woo Kyoung Kim

School of Chemical Engineering, Yeungnam University, Gyeongsan 38541, Republic of Korea

Guy Schmerber, Aziz Dinia, and Silviu Colis†

Institut de Physique et Chimie des Matériaux de Strasbourg (IPCMS), UMR 7504 CNRS-UDS (UDS-ECPM), 23 rue du Loess, BP 43, 67034 Strasbourg Cedex 2, France

(Dated: March 12, 2019)

Abstract

We report on the efficiency improvement of $Cu(InGa)Se_2$ (CIGS) based solar cells obtained upon coating the cell with a Yb-doped SnO_x layer. This layer is deposited by reactive sputtering and serves as a photon down-shifting converter. The direct excitation of the SnO_x host matrix with UV photons leads to a strong emission of near infrared photons from the Yb^{3+} ions suggesting an efficient energy transfer from SnO_x to the Yb^{3+} ions. The deposition the Yb:SnO_x films at higher temperatures results in an enhancement of the PL emission as well as in an improvement of the transport properties. The optimized films exhibit a transmittance around 80 % in the visible region, a resistivity of 6×10^{-3} Ωcm and a mobility as high as 50.1 cm^2/Vs. Such SnO_x layers doped with 1.3 at. % of Yb were deposited at 100°C on conventional CIGS based solar cells to replace the standard ZnO n-type conductive layer. The solar cells performances are noticeably improved. This is witnessed by a net gain of 10% of the external quantum efficiency (EQE) at 360 nm. The short-circuit current (J_{SC}) increased by about 0.56 mA/cm^2 while the fill factor reaches 64.4 %. As an overall result, the best solar cell exhibited a remarkable enhancement in efficiency of about 0.6 %. This improvement of the photovoltaic efficiency by a simple substitution of i-ZnO by Yb:SnO_x for CIGS cells offers possible application to other solar cells. These results are encouraging towards enhancing the efficiency of solar cells at low cost which will contribute to the large deployment of clean energy.

Keywords: CIGS solar cells, Yb-doped SnO_x, down-shifting, energy transfer, sputtering, XPS

*Electronic address: karima.bouras@cea.fr

†Electronic address: colis@ipcms.unistra.fr

I. INTRODUCTION

One of the major issues governing the performances of solar cells is the mismatch between the incident solar radiation spectrum and the absorption of the cell [1, 2]. Because of the weak absorption coefficient of most of the semiconductor absorbers in the UV region, the energy supplied upon absorption of high-energy UV photons cannot be fully converted to electricity and most of energy is lost as heat. This process gives raise to the so-called thermalization losses. At the opposite side of the solar spectrum, infrared photons have energies generally smaller than the band gap of conventional semiconductors (1.1 eV for Si). The solar cell is almost transparent to these photons and additional energy is lost in this way. In order to overcome these issues, two solutions are most frequently investigated. The first solution to limit the losses uses tandem (or multijunction) solar cells in which up to four p-n junctions with different bandgaps are stacked together in order to cover efficiently the solar spectrum. Moreover, when used under concentrated light, such systems may exceed a conversion efficiency of 45 % [3]. A second approach, much less expensive, suggests the use of a photon conversion layer to improve light harvesting and therefore the cell efficiency. Thermalization and transparency losses can be thus considerably reduced [4–7] as the incident solar spectrum matches the absorption of the cell. Rare earths embedded into selected hosts (most often oxides) are used for the different photon management processes: i) down-shifting (DS) or down-conversion (DC) when one high-energy UV photon is converted into one or two low-energy near-infrared photons, and ii) up-conversion (UC) when two low-energy IR photons are converted into one visible photon which can be further absorbed by the solar cell [8–12]. Both conversion processes rely on the luminescence process. For this reason, lanthanides showing intense emission lines due to the intra-4f transitions are ideal dopants for photon management in the conversion layers.

To date, efficient lanthanides-based sensitization has been supplied via host matrices [13–19]. Among the host matrices, oxides are very promising not only for hosting lanthanides but also for their easy integration into the solar cell devices. Due to their low phonon energy they provide a very low rate of non-radiative recombination, promoting the photoluminescence process. While numerous pioneering works have been published on spectral conversion using rare earth doped ZnO and ITO oxide thin films [20–32], SnO_2 has been much less considered as a potential alternative host material. Nevertheless, SnO_2 has a gap of about 3.6 eV (bulk

material), which offers a good absorption in the UV region while being transparent to visible and NIR photons. This is an asset for its integration in solar cells as conversion layers and should not affect the absorption of the cell. More interestingly, SnO_2 has the advantage of combining the above-mentioned optical properties with promising electrical ones. Owing to native oxygen vacancies that can be easily obtained in this system, tin oxide layers can exhibit a large n-type conductivity and carrier concentration [33]. From the conversion point of view, some earlier reports have shed light on the ability of SnO_2 to allow rare-earth doping, notably Nd, Yb, Er, Eu and Sm [34–41]. For all these dopants it was shown that the discrete intermediate levels induced within the gap of the host matrix were involved in intense emission lines.

Among the rare-earth dopants, Yb presents the simplest energy level structure and has been already used in spectral conversion as its NIR emission line matches perfectly with the band gap of the solar cell absorber [41–44]. However, these systems suffer from many issues mainly related to the insertion of lanthanides into the host structure, as the ionic radii of lanthanides and cation from the host oxide are very different. As a consequence, the solubility of rare earth in the host matrix is rather small and oxygen vacancies are generally necessary to make the optical transitions in lanthanides allowed.

Very few reports exist on Yb-doped SnO_2 [45–47]. In this work, we report on the photon conversion of incident UV light to NIR photons in Yb-doped SnO_x sputtered films by taking advantage of the efficient energy transfer from the SnO_x host matrix to the Yb^{3+} ions. The evolution of the structural, electrical and the conversion properties as a function of the deposition temperature is discussed. Finally, by replacing the n-type ZnO conduction layer in a standard $Cu(InGa)Se_2$ (CIGS) solar cell with a Yb-doped SnO_x layer an increase of the cell quantum efficiency is demonstrated. Such an improvement can be understood on the basis of electrical properties improvement and on the down-conversion properties of the Yb-doped SnO_x layer.

II. EXPERIMENTAL DETAILS

A. Yb:SnO_x thin films deposition

Yb-doped SnO_x thin films were deposited using an Orion 3 Radio Frequency (RF) reactive magnetron sputtering from AJA International Co. The deposition was performed on p-type Si(100), quartz substrates and finally on the CIGS/CdS junction of a solar cells. The doping of the SnO_x films with Yb was carried out by placing Yb metal discs (99.99 % from Alfa Aesar Co.) on top of a metallic Sn target (99.99 % from Neyco Co.). During deposition, Ar and O_2 gas flows were fixed to 8 and 5 sccm, respectively. The working pressure and RF power were set at 3.4 mTorr and 50 W, respectively. The substrates are located in top configuration at 12 cm above the target. To insure a good film homogeneity, the substrate holder was in continuous rotation during the deposition process. In order to improve the crystalline quality and thus modulate the electrical and optical properties of the layer, the substrate temperature during the film growth was varied from 100°C to 500°C. The resulting layers have a thickness of about 100 nm. The layers were thoroughly analyzed before integration in solar cells.

B. CIGS-based solar cells fabrication

Molybdenum back contact ($\sim$ 800 nm) was deposited onto glass substrates (2.5×2.5 cm^2) by DC magnetron sputtering. The CIGS absorber layer was grown above by molecular beam epitaxy (MBE) following a three-step procedure. In the first step, an $(InGa)_2Se_3$ film was grown by co-evaporation of In, Ga, and Se at 400°C during 30 min at evaporation rates of 0.19, 0.02, 0.5 nm/s, respectively. In a second step, Cu and Se co-evaporation (rates of 0.09 and 0.5 nm/s) was performed at 550°C for 70 min. CIGS and Cu_xSe are obtained with an excess of Cu and Se. For the final step, extra In, Ga and Se are supplied for 30 min to react with Cu_xSe which resulted in the formation of a single phase CIGS layer with a thickness of about 2.5 μm.

A CdS buffer layer was further deposited on CIGS by chemical bath deposition using a bath of ammonia water, cadmium sulfate and thiourea solution. The solution temperature was increased to 65°C under continuous stirring. The CIGS samples were immersed in the solution during 10 min which led to a CdS film of about 70 nm thick. The samples were then

thoroughly rinsed by de-ionized water, dried under nitrogen gas and annealed at 100°C for 15 min under vacuum. The Yb-doped SnO_2 layer was then deposited by sputtering at 100°C with Ar:O_2 flow ratio of 8:5. The temperature was chosen in order to avoid damaging the cell absorber observed for larger deposition temperatures. The SnO_x layer has a thickness of 20 nm, a resistivity of 9×10^{-4} Ωcm and a carrier concentration of 6.5×10^{20} cm^{-3} to ensure good transport properties. A ZnO:Al layer of about 100 nm was finally deposited atop by DC sputtering at 150°C. In the reference cell, the SnO_x:Yb layer from the front contact was replaced by a i-ZnO layer with a thickness of 80 nm and deposited at room temperature. The Al concentration in ZnO:Al was fixed at 2 at. %. Finally, both set of cells were completed by depositing Ni/Ag as grid using electron beam evaporation at room temperature.

C. Characterization techniques

The crystalline structure of the samples was analyzed by X-ray diffraction using a Rigaku SmartLab diffractometer equipped with a monochromatic source delivering a CuKα_1 incident beam (45 kV, 200 mA, 0.154056 nm). X-ray θ-2θ and reflectivity analyzes were performed in order to check the crystalline quality of the sample, the eventual presence of spurious phases, and determine the film thickness.

Insight into the chemical atomic environment of the different elements (Sn, O, and Yb) and the stoichiometry of the films was obtained by X-ray photoelectron spectroscopy (XPS). The measurements were carried out using a Thermo Electron K-Alpha spectrometer equipped with a monochromatic Al-Kα X-ray source (1486.6 eV). The size of the analyzed spot was about 400 μm. The homogeneity of the sample was checked by measuring on several points on the surface.

The transparency of the films was investigated in the 200-850 nm range using a Perkin-Elmer Lambda 950 spectrophotometer. The photon conversion was checked by photoluminescence (PL) and photoluminescence excitation (PLE) measurements performed in the 360-1050 nm range. For the PL and PLE measurements, the excitation was provided by means of a Nd:YAG laser (355 nm) and a Xenon lamp, respectively. The PL signal was recorded using a cooled CCD camera.

The current-voltage characteristics of the cells were measured under a class AAA K201 McScience solar simulator (AM1.5 irradiation) to extract the photovoltaic parameters such

as the open circuit voltage, the short circuit current and cell efficiency. External quantum efficiency (EQE) measurements were performed using a tungsten halogen lamp as light source and automated filter wheels (41 filters).

III. RESULTS AND DISCUSSION

A. Yb:SnO_x thin films: effect of the deposition temperature

The structural properties of Yb-doped SnO_2 single films deposited on Si(100) substrates have been investigated by X-ray diffraction. All diffractogramms are typical of SnO_2 polycrystalline samples as already reported for other rare earth doped SnO_2 thin films [48]. No spurious phases such as SnO or Yb_2O_3 could be detected in the resolution limit of the XRD technique. Fig. 1 shows the diffraction patterns recorded for a series of samples grown at different temperatures between 100 and 500°C, while all the other deposition parameters remained unchanged. For visibility reasons and in order to have a better insight on the structural evolution induced by the growth temperature the patterns are presented only in the 25-40° 2θ range where the (110) and (200) peaks of SnO_2 are clearly visible. For our samples these peaks are shifted towards smaller angles with respect to their position in undoped SnO_2 (dashed lines in fig. 1) indicating an increase of the lattice parameter due to doping. This can be easily understood if we keep in mind the larger ionic size of Yb^{3+} ion (0.868 Å) with respect to that of Sn^{4+} (0.69 Å) [49]. Another consequence of the peak shift is that, at least partly, Yb ions substitute the Sn ones in the host matrix, most probably involving oxygen vacancies as well. The existence of other types of defects (interstitial ions and oxygen vacancies) is also suggested by the evolution of the diffraction peaks position with the deposition temperature. Indeed, as the temperature increases from 100 to 500°C, the peaks shifts towards higher angles (horizontal arrows (→) in fig. 1) suggesting a more compact and therefore less defected structure. As a consequence the lattice parameter a calculated from the position of the (200) peak decreases progressively from 4.795 to 4.760 ± 0.005 Å, while the crystallite size (average value calculated using both (110) and (200) peaks) slowly increases from 18.5 to 20.5 ± 0.3 nm.

To further investigate the structural changes induced by the increase of the substrate temperature during deposition, XPS analyzes have been carried out. Changes of the atomic

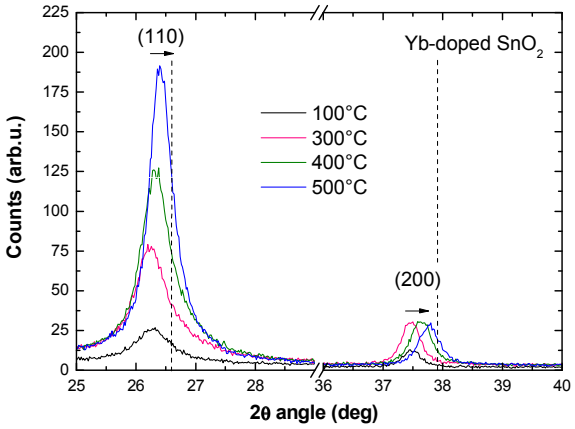

FIG. 1: X-ray diffraction patterns of Yb-doped SnO_2 thin films deposited on Si(100) at different temperatures. The vertical dashed lines indicate the position of the (110) and (200) peaks of undoped SnO_2. The horizontal arrows ($\rightarrow$) indicate the sense of the peak shift while increasing the temperature.

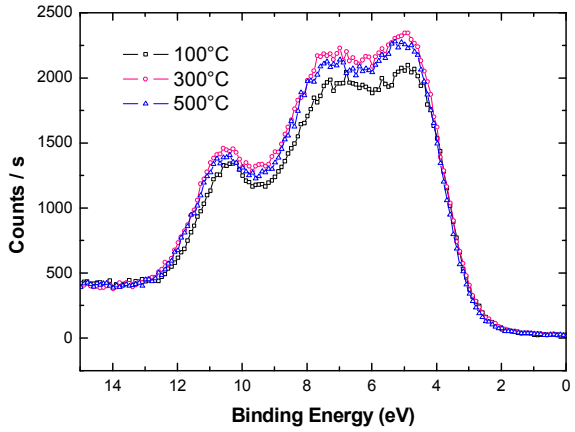

FIG. 2: X-ray photoemission valence bands spectra of the Yb:SnO_2 thin films as a function of the deposition temperature.

environment of the different elements, mainly, Sn, O and Yb can be thus emphasized. The valence bands spectra (fig. 2) were found to perfectly fit the SnO_2 structure, regardless the deposition T, which is in good agreement with the XRD results. At first glance, no peak is observed around 2 eV and, according to different authors, this could indicate the absence of the SnO phase [50].

More details on the tin and oxygen environment can be obtained from the Sn $3d_{5/2}$ and O 1s core levels, respectively. The corresponding spectra are displayed in fig. 3. Surprisingly,

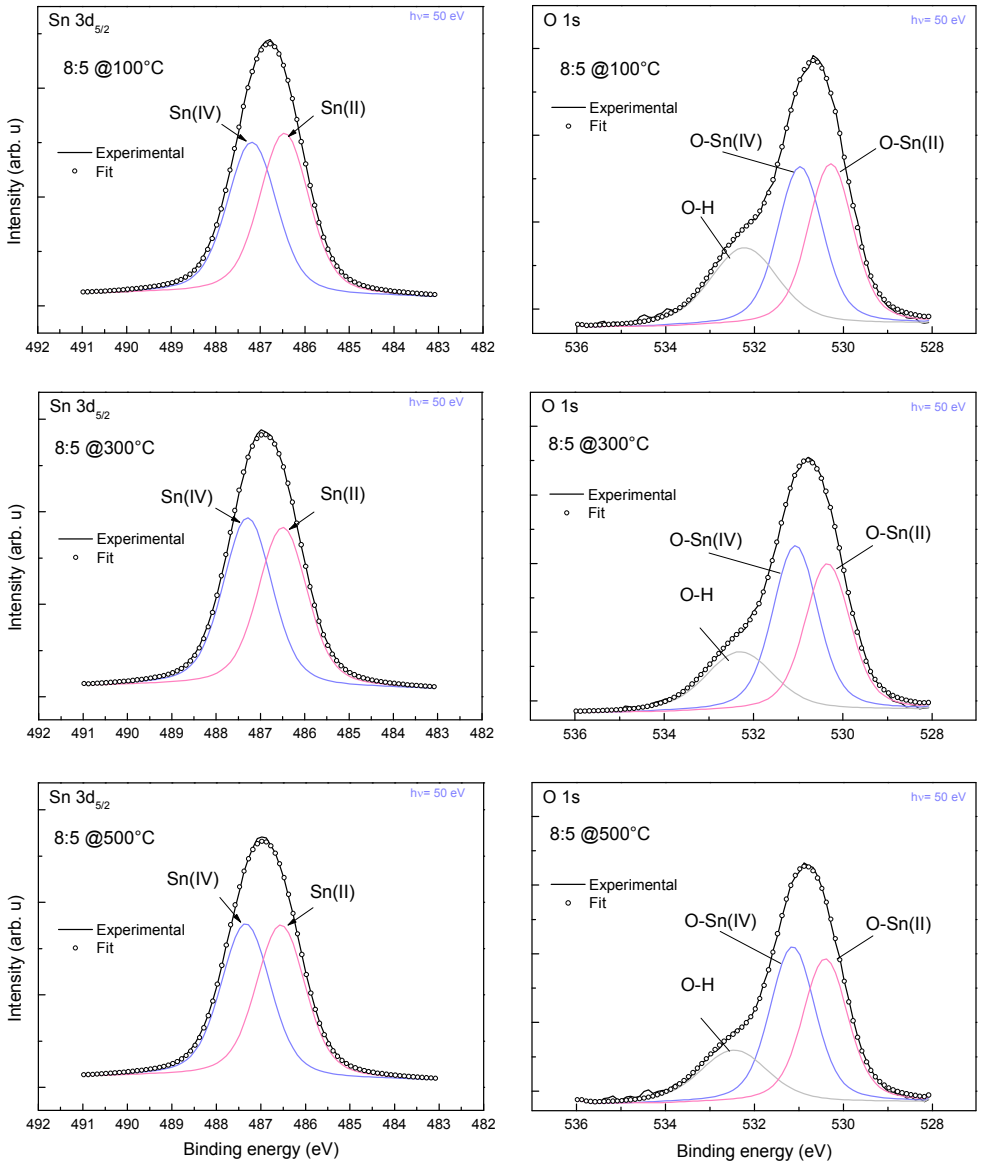

FIG. 3: X-ray photoemission spectra of the $3d_{5/2}$ and 1s core levels of Sn and O, respectively, recorded on Yb-doped SnO_2 films grown at different deposition temperatures.

the deconvolution of both Sn and O core levels reveals the presence of two oxide phases, mainly SnO and SnO_2 with more or less comparable amounts [50–52]. This apparent inconsistency is related to the fact that the kinetic energies of photoelectrons coming from O 1s and Sn $3d_{5/2}$ are lower than the ones of photoelectrons coming for the valence band. It seems therefore possible that the two environments are mainly located at the extreme film surface and that the SnO:SnO_2 ratio calculated from the XPS data is more representative of the first nanometers of the films. This situation is also favored by the reversible dual valence

of Sn and to the presence of the Yb dopant into the structure that substitutes partly Sn^{4+} in SnO_2. All films show almost same SnO:SnO_2 ratio, which is about 50:50 (table I). Although this ratio slightly varies with the deposition temperature, the changes are too small to be significant. It is therefore fair to conclude that the increase of the substrate temperature during the film growth seems to not deeply affect the atomic environment of the elements, and therefore their oxidation state. Table I also reports the oxygen / tin ratio (stoichiometry of the films) which is about 1.6 and decreases slightly when increasing the temperature. This is in agreement with the general behavior of oxides that tend to reduce upon heating. Although this decrease is small, this result will help us understand the photoluminescence properties of the films that will be discussed later in this work.

A similar analysis has been also carried out on the XPS spectra corresponding to the Yb $4d_{5/2}$ core level (fig. 4). At first sight, Yb atoms bounded to oxygen are present in all films whatever the deposition temperature is. This is witnessed by the position of Yb $4d_{5/2}$ peak which is located at about 184.4 eV [53, 54]. Moreover, the Yb $4d_{5/2}$ peak area is quite comparable for all samples, indicating the same density of optically active Yb^{3+} ions. Clearly, the increase of the deposition temperature does not seem to affect the Yb oxidation state. A slight shift towards high binding energies is noticed indicating a slight change in the atomic surroundings of Yb atoms. No Yb^{2+} could be observed in the detection limit of the XPS technique.

The optical properties have been investigated by UV-visible transmission spectroscopy (data not shown here). All the films are found to be transparent over the UV to NIR range with transparencies varying between 80 and 90%. The absorption edges are located

TABLE I: Variation of the SnO and SnO_2 content in Yb-doped SnO_x films deposited at different temperatures (100, 300 and 500°C), extracted from the deconvolution of Sn 3d and O 1s core levels spectra.

Deposition	Sn $3d_{5/2}$ line		O 1s line		Stoichiometry SnO_x
temperature	SnO_2	SnO	SnO_2	SnO	x = [O]/[Sn]
100°C	49.83	50.17	48.41	51.59	1.62 ± 0.01
300°C	51.32	48.68	53.13	46.87	1.58 ± 0.01
500°C	49.99	50.01	52.25	47.75	1.56 ± 0.01

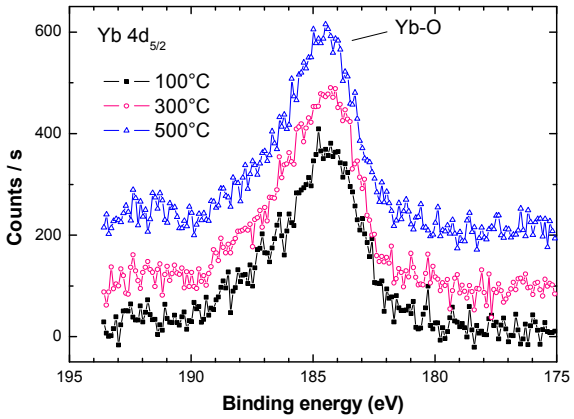

FIG. 4: X-ray photoemission spectra showing the evolution of the Yb $4d_{5/2}$ peak recorded on Yb-doped SnO_2 films grown at different deposition temperatures. The spectra recorded on the samples deposited at 300 and 500°C were shifted along the vertical axis for visibility reasons.

at photon wavelengths lower than 300 nm and are found to shift towards lower wavelengths (high energies) when increasing the deposition temperature, indicating an increase of the band gap. It is interesting to note that except from the 100°C grown film, the other samples exhibit almost same transmission curve, which supports the XPS results in the fact that temperature does not affect significantly the structure of the Yb-doped SnO_x films. The band gap values increase with temperature from 3.56 to 3.82 ± 0.02 eV.

In order to check the optical activity of the dopant, the PL spectra as a function of the deposition temperature were recorded on the Yb-doped SnO_x films and reported in fig. 5. The sample was illuminated with a 355 nm radiation provided by a Nd:YAG laser. Upon excitation, all samples exhibit PL over the UV-Vis-NIR range with different intensities. The film grown at 100°C shows a large UV-visible emission band as well as one intense NIR peak. Different studies on SnO_2 have already shown similar emission bands [55, 56]. The emission band ranging between 380 and 650 nm was attributed to radiative transitions originating from defect states localized within the band gap of the host matrix. As for the NIR peak located at 973 nm it was assigned to radiative transition of 4f-electrons from the $^2F_{5/2}$ excited state to the $^2F_{7/2}$ ground state in Yb^{3+}. A similar intense and narrow peak was also reported in Yb-doped ZnO films [24]. Increasing the substrate temperature during deposition to 300°C did not affect much the emission coming from the host matrix but found to promote that originating from the Yb^{3+} ions. Such behavior indicates a same density

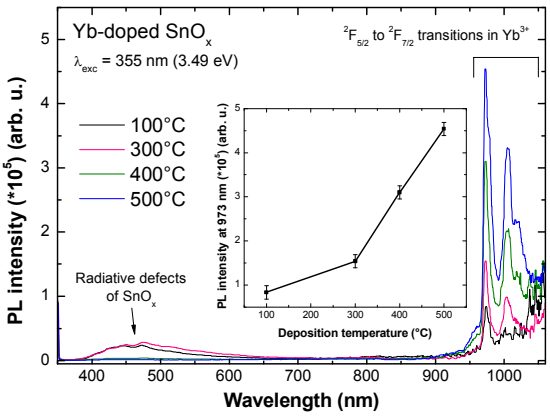

FIG. 5: Photoluminescence spectra of the Yb-doped SnO_x films as a function of the deposition temperature. The inset shows the evolution of PL intensity of Yb recorded at 973 nm.

of radiative defects in the SnO_x structure. The increase of the Yb^{3+} PL (inset of fig. 5) can be understood in terms of atomic environment which becomes, due to temperature, less defected and therefore more favorable to radiative transitions in Yb. At 400 and 500°C, the intensity of the defects emission strongly decreases while that of Yb increases about five times with respect to the one of the sample deposited at 100°C. This is somehow awkward since the XPS data suggested a similar density of Yb^{3+} ions that are optically active in all samples. This result can be however explained by either: i) a decrease of the defects density into the structure related to better crystalline quality, in this case the atomic environment of Yb being much more favorable for its emission), or ii) a transfer of the photon energy arising from transitions within the defects levels to Yb which will increase consequently its emission. It is also interesting to note that for deposition temperatures higher than 100°C, the Yb emission is characterized by the appearance of a second peak at 1030 nm. This is rather surprising but can be explained by the degeneration of the energy levels of Yb^{3+} induced by the crystal field effect of the host matrix. Such wide and intense NIR emission is of interest to solar cells.

In order to investigate the origin of the Yb emission in the NIR region and to understand the energy transfer process, further analyzes by PLE spectroscopy have been performed. The PLE spectra of the Yb-doped SnO_x films as a function of the deposition temperature are presented in fig. 6. The PL intensity of Yb^{3+} ions at 973 nm was monitored while varying the excitation wavelength from 250 to 500 nm. The inset in fig. 6 shows a zoom of the PLE spectra for the samples exhibiting a weak PL intensity. As expected from the PL

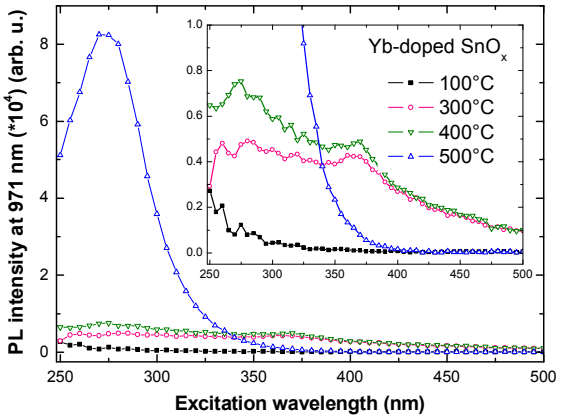

FIG. 6: Photoluminescence excitation spectra of the Yb-doped SnO_x films as a function of the deposition temperature. The inset shows a magnification of the low-intensity spectra region.

results, the PLE spectra show that upon excitation of the host matrix in the UV region, Yb ions simultaneously emit NIR photons. This indicates the presence of an energy transfer occurring from the host SnO_x to the Yb^{3+} rare earth. At 100°C, the energy transfer is found to occur when exciting the matrix between 250 and 350 nm with a maximum intensity at 250 nm. Increasing the deposition temperature to 300°C results in the increase of the Yb emission under excitation in the UV and visible spectral range. This can be seen in the inset in fig. 6, in which the excitation of Yb is extended to 500 nm. As for the sample grown at 500°C, it shows an intense excitation band ranging from 250 to 350 nm with a maximum at 275 nm. Given the different excitation spectra, one could expect different energy transfer mechanisms. Upon excitation of one electron from the valence band to the conduction band of the host, the desexcitation can occur in different ways, either directly to the valence band or to intermediate defect levels within the band gap. This energy of transition is simultaneously transferred to the rare earth in which the 4f-electron will be excited to high energy levels. The desexcitation is then downshifted into NIR emission. Another type of energy transfer is the electronic transfer, in which the electron jumps from one energy level in the host to one excited level of the rare earth [48].

The effect of the growth temperature on the electrical properties of the films was investigated by Hall effect measurements. Overall, the films are of n-type, possess excellent transport properties with resistivities as low 0.006 Ω·cm and carrier concentration as high as 2.28×10^{20} cm^{-3}. The transport properties are generally improved while increasing the

substrate temperature as shown in table II.

B. Integration of Yb:SnO_x layers in CIGS solar cells

Yb-doped SnO_x thin films were deposited onto CIGS solar cells to replace the intrinsic ZnO. A compromise between a good conductivity and a high PL is strongly suited to take advantage of the conversion layer. Thus, the best condition to ensure good transport properties and offer down-shifting functionality without damaging the CdS or CIGS layers is given by the deposition temperature of 100°C. The performances of a reference cell (standard CIGS solar cell) and a cell in which Yb-doped SnO_x replaces the conventional ZnO layer are further compared.

First, external quantum efficiency (EQE) measurements were performed to assess the down-shifting effect provided by the Yb:SnO_x layer. The EQE spectra of both reference and functionalized CIGS cells are shown in fig. 7. As expected, a net gain in the UV region is noted, namely between 300 and 400 nm, due to the conversion of UV photons to NIR ones through down shifting. At 360 nm, the EQE response of the cell is increased to 17.5% against 9.2% for the reference cell. Interestingly, the EQE spectra also show an enhancement over the visible and NIR range. This behavior can be attributed to the improvement of electrical and optical properties of the cell when replacing the ZnO layer with Yb:SnO_x. Although there is no direct proof in this sense, this effect involves more efficient passivation effect, a higher charge carrier collection (better conductivity) and/or a more appropriate reflectance.

To further investigate the performance improvement of the CIGS solar cell induced by the Yb:SnO_x layer, current - voltage dependencies were recorded under standard illumination

TABLE II: Resistivity, carrier concentration and mobility evolution in Yb-doped SnO_x films deposited at different temperatures.

Temperature (°C)	Concentration (cm^{-3})	Resistivity (Ω·cm)	Mobility (cm^2/Vs)
100	4.17×10^{18}	0.0530	28.2
300	1.94×10^{19}	0.0064	50.1
500	2.28×10^{20}	0.0018	14.6

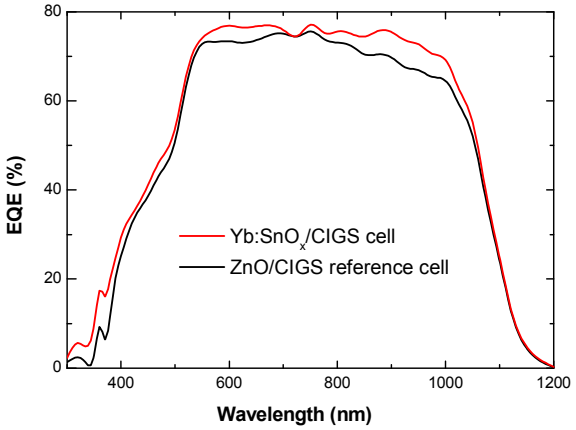

FIG. 7: EQE spectra of a of ZnO/CIGS (reference) and Yb:SnO_x/CIGS solar cells.

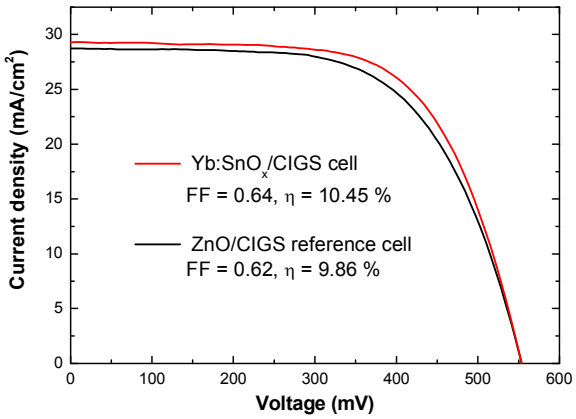

FIG. 8: Voltage dependence of the current density recorded under AM1.5G illumination on ZnO/CIGS (reference) and Yb:SnO_x/CIGS solar cells.

(AM1.5G). The J-V plots are shown in fig. 8 while the extracted photovoltaic parameters are displayed in table III. While the open-circuit voltage (V_{oc}) remains the same for both cells (about 0.55 V), the short circuit current density (J_{sc}) is increased by 0.57 mA/cm^2 as a

TABLE III: Electrical parameters (V_{oc}, I_{sc}, J_{sc}, fill factor and efficiency) of ZnO/CIGS (reference) and Yb:SnO_x/CIGS solar cells.

Cell	V_{oc} (V)	I_{sc} (mA)	J_{sc} (mA/cm^2)	FF (%)	η (%)
ZnO/CIGS (reference)	0.55	14.64	28.72	62.03	9.86
Yb:SnO_x/CIGS	0.55	14.93	29.28	64.43	10.45

consequence of the photon conversion provided by the Yb:SnO_x layer. As for the fill factor (FF), its value increases by 2.4 % due to the good electrical properties of the conversion layers. More precisely, our SnO_x and Yb:SnO_x possess good transport properties compared to i-ZnO used for the reference cell. Indeed, the measured series resistance decreases from 3.68 Ωcm^2 for the reference cell to 3.30 Ωcm^2 for the Yb:SnO_x based cell. As a consequence, the solar cell efficiency is enhanced by about 0.6 %, which is quite remarkable. Such result is an obvious proof of the potential of Yb:SnO_x layers for solar cells performance enhancement and can constitute a viable low-cost solution for a wide range of solar cells where down-shifting layers could be integrated. *Finally note that the J_{sc} values measured from the J-V curves (28.72 and 29.28 mA/cm^2 for the ZnO/CIGS and Yb:SnO_x/CIGS cells, respectively - see table III) match very well the values determined from the spectral response (28.30 and 29.68 mA/cm^2 for the ZnO/CIGS and Yb:SnO_x/CIGS cells, respectively). This supports the reliability of the measurements and that of the analyzed system. The small differences can be explained in terms of charge recombination, heating or passivation differences during the J-V and EQE experiments.*

IV. CONCLUSION

Yb-doped SnO_x layers were obtained by RF magnetron sputtering at different temperatures ranging from 100 to 500°C. The films are polycrystalline and strongly substoichiometric ($x = 1.6$). They showed a reduced resistivity in the 10^{-3} Ωcm range and a large electron mobility that can reach 50.1 cm^2/Vs. XPS and PL measurements indicated the presence of Yb^{3+} ions that are optically active. An energy transfer occurring between the host SnO_x and the Yb ions is demonstrated through PLE measurements. The Yb-doped SnO_x optimized layers were integrated to CIGS solar cells to replace conventional ZnO. A net increase of the EQE response is noticed. In the UV region this is explained on the basis of down shifting process while in the NIR range this is due to electrical factors (passivation, resistivity, and mobility improvement). The electrical measurements show no change in V_{oc} but an increase in the J_{sc} and FF with about 0.56 mA/cm^2 and 2.4 %, respectively. Finally, the conversion efficiency of the CIGS-based cell is enhanced by about 0.6 %, which is extremely encouraging for future implementation of such low cost converting layers in photovoltaic technology.

Acknowledgments

K.B. acknowledges the Région Alsace and the INSA of Strasbourg for financial support.

---

[1] L.C. Hirst and N.J. Ekins-Daukes, Fundamental losses in solar cells, Prog. Photovolt: Res. Appl. 19 (2011) 286293.

[2] D. Chen, Y. Wang, M. Hong, Lanthanide nanomaterials with photon management characteristics for photovoltaic application, Nano Energy 1 (2012) 73-90.

[3] F. Dimroth, T.N.D. Tibbits, M. Niemeyer, F. Predan, P. Beutel, C. Karcher, E. Oliva, G. Siefer, D. Lackner, P.F. Kailuweit, A.W. Bett, R. Krause, C. Drazek, E. Guiot, J. Wasselin, A. Tauzin, T. Signamarcheix, Four-junction wafer-bonded concentrator solar cells, IEEE J. Photovoltaics 6 (2016) 343-349.

[4] T. Trupke, M.A. Green, P. Würfel, Improving solar cell efficiencies by down-conversion of high-energy photons, J. Appl. Phys. 92 (2002) 1668-1674.

[5] T. Trupke, M.A. Green, P. Würfel, Improving solar cell efficiencies by up-conversion of sub-band-gap light, J. Appl. Phys. 92 (2002) 4117-4122.

[6] T. Trupke, A. Shalav, B.S. Richards, P. Würfel, M.A. Green, Efficiency enhancement of solar cells by luminescent up-conversion of sunlight, Solar Energy Materials and Solar Cells 90 (2006) 3327-3338.

[7] R.A. Ze'ev, A. Niv, X. Zhang, Solar energy enhancement using down-converting particles: A rigorous approach, J. Appl. Phys. 109 (2011) 114905.

[8] H.Q. Wang, M. Batentschuk, A. Osvet, L. Pinna, C.J. Brabec, Rare-earth ion doped up-conversion materials for photovoltaic applications, Adv. Mater. 23 (2011) 2675-2680.

[9] B.S. Richards, Luminescent layers for enhanced silicon solar cell performance: Down-conversion, Solar Energy Materials and Solar Cells 90 (2006) 1189-1207.

[10] A. Shalav, B.S. Richards, M.A. Green, Luminescent layers for enhanced silicon solar cell performance: Up-conversion, Solar Energy Materials and Solar Cells 91 (2007) 829-842.

[11] G. Chen, J. Seo, C. Yang, P.N. Prasad, Nanochemistry and nanomaterials for photovoltaics, Chemical Society Reviews 42 (2013) 8304-8338.

[12] A. Gavriluta, T. Fix, A. Nonat, A. Slaoui, J.F. Guillemoles, L.J. Charbonniere, Tuning the

chemical properties of europium complexes as downshifting agents for copper indium gallium selenide solar cells, J. Mater. Chem. A 5 (2017) 14031-14040.

[13] J.C.G. Bünzli, A.S. Chauvin, Chapter 261 - Lanthanides in Solar Energy Conversion, in: G.B. Jean-Claude, K.P. Vitalij (Eds.) Handbook on the Physics and Chemistry of Rare Earths, Elsevier, vol. 37 (2014) 169-281.

[14] H. Lian, Z. Hou, M. Shang, D. Geng, Y. Zhang, J. Lin, Rare earth ions doped phosphors for improving efficiencies of solar cells, Energy 57 (2013) 270-283.

[15] J.C.G. Bünzli, S. Comby, A.S. Chauvin, C.D.B. Vandevyver, New opportunities for lanthanide luminescence, J. Rare Earths 25 (2007) 257-274.

[16] E. Hemmer, N. Venkatachalam, H. Hyodo, A. Hattori, Y. Ebina, H. Kishimoto, K. Soga, Up-converting and NIR emitting rare earth based nanostructures for NIR-bioimaging, Nanoscale 5 (2013) 11339-11361.

[17] J.C.G. Bünzli, S.V. Eliseeva, Lanthanide NIR luminescence for telecommunications, bioanalyses and solar energy conversion, J. Rare Earths 28 (2010) 824-842.

[18] M. Nyk, R. Kumar, T.Y. Ohulchanskyy, E.J. Bergey, P.N. Prasad, High contrast in vitro and in vivo photoluminescence bioimaging using near infrared to near infrared up-conversion in Tm^{3+} and Yb^{3+} doped fluoride nanophosphors, Nano Lett. 8 (2008) 3834-3838.

[19] A.J. Kenyon, Recent developments in rare-earth doped materials for optoelectronics, Progress in Quantum Electronics 26 (2002) 225-284.

[20] C. Fu, J. Liao, W. Luo, R. Li, X. Chen, Emission of 1.53 μm originating from the lattice site of Er^{3+} ions incorporated in TiO_2 nanocrystals, Opt. Lett. 33 (2008) 953-955.

[21] Y. Liu, W. Luo, R. Li, X. Chen, Optical properties of Nd^{3+} ion-doped ZnO nanocrystals, J. Nanoscience and Nanotechnology 10 (2010) 1871-1876.

[22] Q. Yin, X. Jin, G. Yang, C. Jiang, Z. Song, G. Sun, Biocompatible folate modified Gd^{3+}/Yb^{3+}-doped ZnO nanoparticles for dualmodal MRI/CT imaging, RSC Advances 4 (2014) 53561-53569.

[23] J. Zhang, S.J. Deng, S.Y. Liu, J.M. Chen, B.Q. Han, Y. Wang, Y.D. Wang, Preparation and photocatalytic activity of Nd doped ZnO nanoparticles, Materials Technology 29 (2014) 262-268.

[24] M. Balestrieri, G. Ferblantier, S. Colis, G. Schmerber, C. Ulhaq-Bouillet, D. Muller, A. Slaoui, A. Dinia, Structural and optical properties of Yb-doped ZnO films deposited by magnetron

reactive sputtering for photon conversion, Solar Energy Materials and Solar Cells 117 (2013) 363-371.

[25] M. Balestrieri, M. Gallart, M. Ziegler, P. Bazylewski, G. Ferblantier, G. Schmerber, G.S. Chang, P. Gilliot, D. Muller, A. Slaoui, S. Colis, A. Dinia, Luminescent properties and energy transfer in Pr^{3+} doped and Pr^{3+}-Yb^{3+} co-doped ZnO thin films, J. Phys. Chem. C 118 (2014) 13775-13780.

[26] R. Elleuch, R. Salhi, J.L. Deschanvres, R. Maalej, Highly efficient NIR to visible upconversion in a ZnO:Er,Yb thin film deposited by a AACVD atmospheric pressure process, RSC Advances 5 (2015) 60246-60253.

[27] G. Gottardi, R. Pandiyan, V. Micheli, G. Pepponi, S. Gennaro, R. Bartali, N. Laidani, Effect of Nd^{3+} incorporation on the microstructure and chemical structure of RF sputtered ZnO thin films, Mater. Sci. Eng. B 178 (2013) 609-616.

[28] Y. Liu, C. Xu, Q. Yang, White upconversion of rare-earth doped ZnO nanocrystals and its dependence on size of crystal particles and content of Yb^{3+} and Tm^{3+}, J. Appl. Phys. 105 (2009) 084701.

[29] I. Soumahoro, G. Schmerber, A. Douayar, S. Colis, M. Abd-Lefdil, N. Hassanain, A. Berrada, D. Muller, A. Slaoui, H. Rinnert, Structural, optical, and electrical properties of Yb-doped ZnO thin films prepared by spray pyrolysis method, J. Appl. Phys. 109 (2011) 033708.

[30] X. Wei, W. Wang, K. Chen, ZnO:Er,Yb,Gd particles designed for magnetic-fluorescent imaging and near-infrared light triggered photodynamic therapy, J. Phys. Chem. C 117 (2013) 23716-23729.

[31] Y.P. Du, Y.W. Zhang, L.D. Sun, C.H. Yan, Efficient energy transfer in monodisperse Eu-doped ZnO nanocrystals synthesized from metal acetylacetonates in high-boiling solvents, J. Phys. Chem. C 112 (2008) 12234-12241.

[32] M.H. Choi, T.Y. Ma, Erbium concentration effects on the structural and photoluminescence properties of ZnO:Er films, Materials Lett. 62 (2008) 1835-1838.

[33] D.A. Keller, H.N. Barad, K.J. Rietwyk, A. Ginsburg, E. Borvick, M. Priel, A.Y. Anderson, S. Meir, A. Zaban, Oxygen concentration as a combinatorial parameter: The effect of continuous oxygen vacancy variation on SnO_2 layer conductivity, Materials Chemistry and Physics 208 (2018) 289-293.

[34] W. Chen, Y. Liu, Z. Qin, Y. Wu, S. Li, N. Gong, Improved ethanediol sensing with single Yb

ions doped SnO_2 nanobelt, Ceramics International 42 (2016) 10902-10907.

[35] H. Bastami, E. Taheri-Nassaj, Synthesis of nanosized (Co, Nb, Sm)-doped SnO_2 powders using co-precipitation method, J. Alloys and Compounds, 495 (2010) 121-125.

[36] E. Cao, Y. Zhang, W. Hao, H. Peng, L. Sun, J. Hu, Room temperature ferromagnetism in Sm-doped SnO_2 PLD film, Appl. Surf. Sci. 282 (2013) 376-383.

[37] W.Q. Li, S.Y. Ma, Y.F. Li, X.B. Li, C.Y. Wang, X.H. Yang, L. Cheng, Y.Z. Mao, J. Luo, D.J. Gengzang, G.X. Wan, X.L. Xu, Preparation of Pr-doped SnO_2 hollow nanofibers by electrospinning method and their gas sensing properties, J. Alloys and Compounds 605 (2014) 80-88.

[38] F. Hild, L. Eichenberger, A. Bouché, X. Devaux, M. Stoffel, H. Rinnert, M. Vergnat, Structural and photoluminescence properties of evaporated SnO_2 thin films doped with rare earths, Energy Procedia 84 (2015) 141-148.

[39] K. Bouras, G. Schmerber, D. Aureau, H. Rinnert, G. Ferblantier, T. Fix, S. Colis, P. Bazylewski, B. Leedahl, A. Etcheberry, G.S. Chang, A. Dinia, A. Slaoui, Insight into photon conversion of Nd^{3+} doped low temperature grown p and n type tin oxide thin films, RSC Adv. 6 (2016) 67157-67165.

[40] B. Cojocaru, D. Avram, V. Kessler, V. Parvulescu, G. Seisenbaeva, C. Tiseanu, Nanoscale insights into doping behavior, particle size and surface effects in trivalent metal doped SnO_2, Sci. Rep. 7 (2017) 9598.

[41] H. Dong, L.D. Sun, Y.F. Wang, J.W. Xiao, D. Tu, X. Chen, C.H. Yan, Photon upconversion in Yb^{3+}-Tb^{3+} and Yb^{3+}-Eu^{3+} activated core/shell nanoparticles with dual-band excitation, J. Mater. Chem. C 4 (2016) 4186-4192.

[42] K. Prorok, M. Pawlyta, W. Stręk, A. Bednarkiewicz, Energy migration up-conversion of Tb^{3+} in Yb^{3+} and Nd^{3+} codoped active-core/active-shell colloidal nanoparticles, Chem. Mater. 28 (2016) 2295-2300.

[43] A. Nadort, J. Zhao, E.M. Goldys, Lanthanide upconversion luminescence at the nanoscale: fundamentals and optical properties, Nanoscale 8 (2016) 13099-13130.

[44] L. Marciniak, K. Prorok, L. Frances-Soriano, J. Perez-Prieto, A. Bednarkiewicz, A broadening temperature sensitivity range with a core-shell YbEr@YbNd double ratiometric optical nanothermometer, Nanoscale 8 (2016) 5037-5042.

[45] C. Bouzidi, H. Elhouichet, A. Moadhen, Yb^{3+} effect on the spectroscopic properties of Er-Yb

codoped SnO_2 thin films, J. Luminescence 131 (2011) 2630-2635.

[46] E. Callone, G. Carturan, Y. Jestin, M. Ferrari, Synthesis improvement of Yb^{3+}-activated SnO_2 nanocrystals, Solid State Phenomena 128 (2007) 31-40.

[47] T.T. Wang, S.Y. Ma, L. Cheng, J. Luo, X.H. Jiang, W.X. Jin, Preparation of Yb-doped SnO_2 hollow nanofibers with an enhanced ethanol-gas sensing performance by electrospinning, Sensors and Actuators B: Chemical 216 (2015) 212-220.

[48] K. Bouras, G. Schmerber, H. Rinnert, D. Aureau, H. Park, G. Ferblantier, S. Colis, T. Fix, C. Park, W.K. Kim, A. Dinia, A. Slaoui, Structural, optical and electrical properties of Nd-doped SnO_2 thin films fabricated by reactive magnetron sputtering for solar cell devices, Solar Energy Materials and Solar Cells 145 (2016) 134-141.

[49] R.D. Shannon, Revised effective ionic radii and systematic studies of interatomic distances in halides and chaleogenides, Acta Cryst. A 32 (1976) 751.

[50] J.M. Themlin, M. Chtaïb, L. Henrard, P. Lambin, J. Darville, J.M. Gilles, Characterization of tin oxides by x-ray-photoemission spectroscopy, Phys. Rev. B 46 (1992) 2460-2466.

[51] J.M. Themlin, R. Sporken, J. Darville, R. Caudano, J.M. Gilles, R.L. Johnson, Resonant-photoemission study of SnO_2: Cationic origin of the defect band-gap states, Phys. Rev. B 42 (1990) 11914-11925.

[52] C.L. Lau and G.K. Wertheim, Oxidation of tin: an ESCA study, J. Vac. Sci. Technol. 15 (1978) 622-624.

[53] F. Rivera-López, M. Pérez, X-ray photoelectron spectroscopy: surface and depth profiling studies of glasses doped with Nd and Yb ions, Surface and Interface Analysis 44 (2012) 927-930.

[54] S. Schmidt, S. Hüfner, F. Reinert, W. Assmus, X-ray photoemission of $YbInCu_4$, Phys. Rev. B 71 (2005) 195110.

[55] F. Gu, S.F. Wang, M.K. Lü, G.J. Zhou, D. Xu, D.R. Yuan, Photoluminescence properties of SnO_2 nanoparticles synthesized by sol-gel method, J. Phys. Chem. B 108 (2004) 8119-8123.

[56] F. Gu, S.F. Wang, M.K. Lü, X.F. Cheng, S.W. Liu, G.J. Zhou, D. Xu, D.R. Yuan, Luminescence of SnO_2 thin films prepared by spin-coating method, J. Crystal Growth 262 (2004) 182-185.